ORIGINAL ARTICLE

An efficient closed-form solution for springback prediction and compensation in elastic–plastic creep age forming

Xi Wang[1] · Qi Rong[1] · Zhusheng Shi[1] · Jianguo Lin[1]

Abstract

Accurately predicting the amount of springback has always been a prior focus in metal forming industry, particularly for creep age forming (CAF), for its significant effect on tool cost and forming accuracy. In this study, a closed-form solution for CAF springback prediction covering deformation from elastic to plastic loadings was developed by combining the beam theory and Winkler's theory, based on which an efficient springback compensation method for CAF was proposed. This developed solution extends the application area beyond the traditional beam theory-based springback prediction methods, maintaining its validity with large loading deflection in plastic range. Finite element (FE) simulation and four-point bending CAF tests adopting a 3rd generation Al-Li alloy were conducted in both elastic and plastic forming regions and the results showed close agreement with the closed-form springback predictions. For the proposed compensation method, an adjustment factor was introduced for complex flexible tool CAF to consider its deviation from the uniform stress loading and can be obtained using the closed-form solution. The flexible tool CAF tests using the Al-Li alloy demonstrated the applicability of the proposed compensation method to obtain the target shape within reasonable iterations, which can be further reduced by combining FE simulation.

Keywords Springback prediction · Springback compensation · Closed-form solution · Creep age forming · Al-Li alloy · Multipoint flexible tool

Nomenclature

a, a'	Compensation factor for modified displacement adjustment method and adjustment factor for the solution-based springback compensation method	E	Young's modulus of the material
		f_c	Adopted constitutive model for creep-ageing
$C^i, C^{i+1}, C^j, C^{j+1}$	Tool shape C in the ith and $(i+1)^{th}$, j^{th} and $(j+1)^{th}$ iterations respectively for displacement adjustment and modified displacement adjustment methods	I	Moment inertia of yz plane for z axis
		k_1, k_2, k_3	Curvatures of sheet element in elastic loading, at the end of elastic loading, and in plastic loading, respectively
D	Target shape to be formed	L, L_1	Distance between supporting points and distance between the supporting and loading points
d_{ll}, d_{lm}, d'_{lm}	Loading displacements at the loading points (four-point bending), at the midpoint, and at the midpoint adopting the flexible tool	M_1, M_2, M_3	Moments generated in local yz plane for z axis in elastic loading, at the end of elastic loading, and in plastic loading
		M_{load}, M_{end}	Moments in yz plane for z axis at the end of loading stage and at the end of creep-ageing stage after stress relaxation before unloading
d_{rl}, d_{rm}	Springback recovered deflection at loading points (four-point bending) and at the midpoint	O_a, O_b	Centre points of loaded curvature and CAFed, i.e. final deformed curvature of the sheet

✉ Zhusheng Shi
zhusheng.shi@imperial.ac.uk

[1] Department of Mechanical Engineering, Imperial College London, London SW7 2AZ, UK

🍊 Springer

O_1, O_2, O_3	Centre points of sheet segment with the polar coordinate in elastic loading, at the end of elastic loading, in plastic loading
R_a, R_b, R_c	Curvature radii of loaded shape, CAFed shape, and target shape
R_{n1}, R_{n2}, R_{n3}	Distances of the neutral plane to the origin point O_1 in elastic loading, and to the origin point O_2 at the end of elastic loading and in plastic loading, respectively
r, r_i, r_o	Distance of random specific plane to the origin point. Distances of the top and bottom elastic–plastic boundary to the origin point O_2 in plastic loading state
S^i, S^j	Obtained formed shape S in i^{th} and j^{th} iterations
t	Sheet thickness
t_a	A certain time point during creep-ageing
Tol_1	Error tolerances respectively for modified springback compensation method
x, y, z	Local Cartesian coordinate system, in which y- and z-axes form the plane perpendicular to the neutral plane, and x axis locates at centroid of yz plane and is parallel to the neutral plane
x', y', z'	Axes parallel to the length, thickness, and width directions of the specimen with the origin at the centre point of the specimen bottom surface
y_d	Distance of layer d of the sheet to the neutral plane
Δd_f	Deflection at midpoint of the CAFed sheet compared with its undeformed initial state
Δe	The shape error at midpoint between the CAFed and target shape of the sheet
$\Delta\theta, \Delta\varepsilon, \Delta M$	Increments of the centre angle, strain, and moment in the transformation process from $a_2b_2c_2d_2$ to $a_3b_3c_3d_3$
$\varepsilon, \varepsilon_2, \varepsilon_y$	Strain generated along x direction, accumulated strain at the end of elastic loading, and strain at 0.1% offset yielding point
$\varepsilon_c, \varepsilon_e, \varepsilon_p$	Accumulated creep strain, elastic strain, and plastic strain along x direction
$\theta, \theta_a, \theta_b$	Centre angle of the sheet segment. Centre angles of loaded curvature and CAFed curvature of the sheet
$\theta_1, \theta_2, \theta_3$	Centre angles of deformed segment in elastic loading, at the end of elastic loading, and in plastic loading
$\sigma, \sigma_e, \sigma_p$	Stress along x direction, stress at layer r along x direction in elastic region and plastic region in plastic loading, respectively
σ_r	Relaxed stress along x direction in yz plane

1 Introduction

Creep age forming (CAF) is a metal forming method specially invented for fabricating large-scale aluminium alloys' panel components. Normally CAF process is comprised of three stages, i.e. loading, creep-ageing, and unloading. Deformation in CAF resulted by creep strain evolution can be induced below yield strength of the material. When compared with other traditional metal forming methods for panel fabrication, CAF has its advantages to obtain the final deformed panel [1]. However, springback is still unavoidable. Therefore, accurately predicting the springback becomes the key of applying CAF to deform panel with target shape/curvature. In the recent decade, advanced constitutive models have been proposed to more accurately predict creep deformation [2–4], and improved adjustable forming tool was developed to facilitate obtaining formed panel with target curvature in CAF [5]. Nevertheless, large springback occurring in unloading stage due to the limited portion of creep strain accumulated in creep-ageing stage presents a strong challenge for tool shape design, which significantly affects the tooling cost and the efficiency of fabricating CAF panels with the required curvature [6].

Springback happens in the unloading stage of metal forming as a result of recovery of elastic strain induced in loading stage, which has long been a focus in the whole metal forming field due to its substantial association with forming accuracy and fabrication efficiency. In the past decades, as reviewed by Wagoner et al. [7], analytical solutions and methods utilising finite element (FE) analysis were proposed to predict springback regarding to different metal forming conditions such as pure bending [8], bending combined with tension [9, 10], and draw bending [11, 12]. Additionally, in recent years, investigation of springback has extended to the non-linear plastic bending behaviour with large deformation [13], bending of curved beam and tube [14, 15], and multiple reciprocating bending [16]. In the area of CAF, early investigation of springback analysis was conducted based on Euler–Bernoulli beam theory for predicting the formed sheet shape in single-curvature case [17]. Latterly by independently considering relations of moment and bending curvature derived from the beam theory along length and width directions, prediction of springback for double-curvature bending was fulfilled [18]. With the development

of constitutive model for creep-ageing, by adopting the mechanism-based model to reflect stress-creep strain relationship in CAF, Jeunechamps et al. [19] further proposed an analytical springback prediction method which can be applied to double-curvature bending case of CAF sheet. Li et al. [20] further extended the application of springback prediction surpassing elastic region, by utilising the beam theory and FE analysis.

In practical fabrication, the idea of springback control by compensating tool shape to achieve the target shape/curvature has been widely adopted. Displacement adjustment (DA) method, initially proposed by Gan et al. [21], is a direct geometric iterative control method by continually adjusting tool shape to let shape/curvature of the formed sheet gradually approaching the target value. Figure 1 shows schematically the DA method. The iterative algorithm of the DA method can be expressed as:

$$C^{i+1} = C^i - (S^i - D) \qquad (1)$$

where C^i and S^i are the tool shape and the deformed shape after springback in i^{th} iteration, and D is the target shape to be formed. Hence the term $(S^i - D)$ can be viewed as the geometric error between the deformed and target shape in i^{th} iteration as shown in Fig. 1b. C^{i+1} is the tool shape taken in the $(i+1)^{th}$ fabrication iteration, as demonstrated in Fig. 1c, which is directly obtained by compensating the tool shape C^i in previous i^{th} iteration with the geometric error $(S^i - D)$.

Based on the proposed DA method and utilising FE simulation, satisfactory convergence was reported to have been achieved between the shape of the sheet and its target surface formed by compensated flexible dies [22]. By considering compensation direction, Yang and Ruan [23] applied the DA method for the case of stamping of high strength steel, in which large displacement and rotation can occur during springback. In their study, errors between experimental and FE simulation results were observed after completion of one iteration. When the tool shape C and deformed sheet shape S were obtained from FE results to replace experimental ones, the validity of the DA method becomes highly dependent on the accuracy of simulated springback prediction results [7]. Hence the simulation error can become an issue for adopting FE analysis as an alternative tool, especially for fabrication of components requiring high precision. On the other hand, when the values of C and S are determined

from experimental results without proper analytical method, it can be highly time-consuming and costly on approaching the target value by iterations. It is of significance to find the balance between prediction accuracy of springback and cost of practical experiments to ensure the validity and effectiveness of the DA method.

Efforts have been made to seek progresses in DA method, aiming at reducing iterations and speeding up the convergence to deform the sheet to target shape [24, 25]. The variation of the DA method can be generalised as:

$$C^{j+1} = C^j - \alpha(S^j - D) \qquad (2)$$

By introducing a compensation factor α in the equation, the geometric error $(S^j - D)$ in j^{th} iteration is revised to speed up the convergence rate and to broaden its application in complex cases such as deforming with varied curvature. The value of the compensation factor α is highly dependent on the material, forming process and geometry of the forming tool [26]. As a result, α can be different in each iteration and unpredictable, especially in the case of nonlinear forming with varying curvature [20]. To approach a proper value of α, a secant method was proposed by Li et al. [20] in recent study.

With continued advancements in new generation aluminium alloys possessing superior mechanical properties, these high strength aluminium alloys have been widely adopted in practical fabrication recently [27]. Among these high strength alloys, the latest 3rd generation Al-Li alloy has drawn much attention and is being viewed as a competitive substitution of its predecessors for its balanced synergy of strength, weight reduction, toughness, and corrosion resistance [28]. However, with the prominent strength promotion for this Al-Li alloy, the creep resistance is enhanced simultaneously which in turn reduces the creep deformation in CAF: limited creep strain was observed in creep-ageing for this alloy [29]. Consequently, plastic strain can be needed and be introduced through large deformation in loading stage as supplement for CAF of the material. Hence, due to the required high stress in creep-ageing for the Al-Li alloy and large deformation in loading stage, the applicability of the beam theory for springback prediction may be limited. When large deformation is exerted which induces plastic region in outer bending layers of the forming sheet, the Euler–Bernoulli beam theory, established within elastic region with assumption of small deflection, becomes inappropriate to

Fig. 1 Schematic of DA method for springback compensation

(a) Loaded to tool shape C^i (b) Geometric error $(S^i - D)$ (c) Loaded to tool shape C^{i+1}
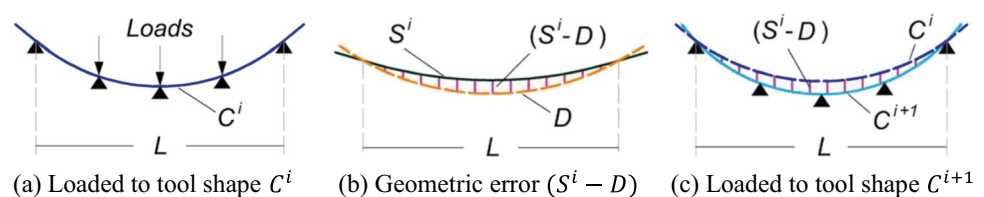
describe deflection and induced stress: the relation of bending strain ε and curvature k can lose its geometry validity in the case of large deformation. Hence a new analytical method to properly reflect the stress states of material in large deformation for CAF with high strength Al-Li alloys is urgently required, based on which the prediction accuracy of springback and the validity of corresponding developed compensation method can be ensured.
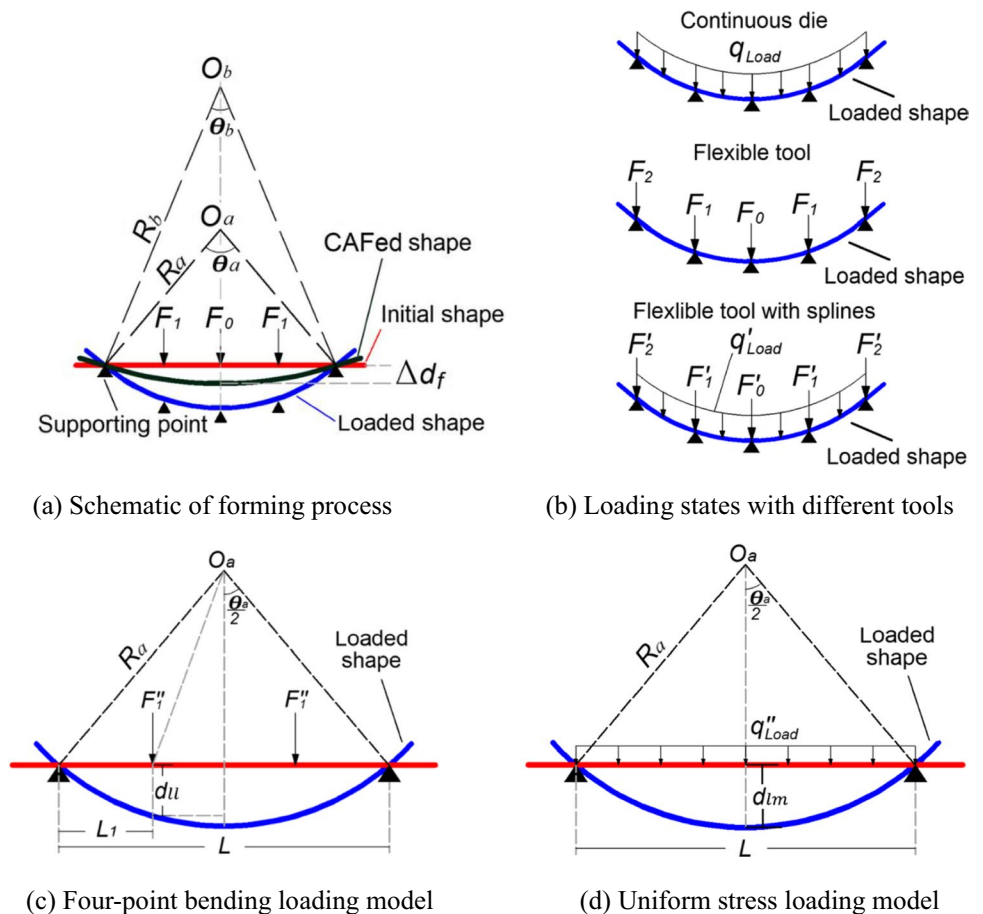
To fill the gap of analytical springback prediction in CAF with large loading displacement, a closed-form prediction solution covering constitutive relations from elastic to plastic in CAF is developed in this study by combining the beam theory and Winkler's theory. The solution is verified with four-point bending CAF tests adopting the latest 3rd generation Al-Li alloy. To improve the efficiency in experimental iterations and solve the accuracy issue raised by prediction error from FE analysis, an efficient springback compensation method, based on the developed springback prediction solution, is proposed by introducing an adjustment factor for CAF with complex flexible tool. The effectiveness and adaptivity of the proposed method are verified through CAF of targeted single-curvature sheets by using flexible tool and the same Al-Li alloy with different thicknesses.

2 Closed-form solution of CAF springback prediction

2.1 Geometric relation in CAF of single curvature sheet

In practical CAF fabrication, metal sheets are formed in forming tools with designed curvature, which can be continuous upper and lower dies, lower supporting dies/ribs in vacuum autoclave, or flexible tool with multiple loading and supporting points. Figure 2a schematically shows the sheet shape at various CAF stages. (i) Initially, the sheet is placed and supported on the forming tool, shown as the red initial shape. (ii) Then the downward loads/displacement (F_0, F_1, etc.) are applied and the sheet is deformed to the designed loaded shape in blue. O_a is the centre point of the loaded shape with curvature radius R_a, and θ_a is the centre angle for the loaded curvature between the two supporting points on the edges. (iii) After deforming to the loaded shape, the sheet is kept in this shape and creep-aged at elevated temperature for designed ageing time. (iv) Finally, the sheet is unloaded after completion of creep-ageing and the final CAFed sheet is obtained after

Fig. 2 Schematic of forming in CAF fabrication and two proposed loading models

(a) Schematic of forming process

(b) Loading states with different tools

(c) Four-point bending loading model

(d) Uniform stress loading model

springback. As shown in Fig. 2a, the CAFed sheet has a curvature radius of R_b with O_b as the centre point and θ_b as the centre angle for the final CAFed shape. Δd_f is the deflection at midpoint of the final CAFed sheet from its initial undeformed state.

Figure 2b illustrates schematically the loading states with different forming tools. For loading with continuous die or autoclave vacuum, the load is applied in the form of pressure and can be treated as a line load q_{Load} when considering unit width. When adopting multipoint flexible tool, the sheet is deformed with multiple point loads F_x. When deforming with a flexible tool, elastic pads/splines are normally added between loading points and forming sheet to achieve more uniformly distributed stress and smoother forming curvature, thus minimising surface damages [20, 22, 30]. Therefore, as shown in Fig. 2b, the loading state for flexible tool with splines can be treated as combination of point loads F'_x and line load q'_{load}. Furthermore, when CAF fabrication is conducted in complex forming tool, the loaded structure is in hyperstatic state which significantly raises the difficulty of stress analysis for the deforming sheet. To simplify the analysis procedure, as demonstrated in Fig. 2c and d, fundamental loading models, i.e. four-point bending with two supporting and loading points and uniformly distributed stress bending, are adopted for the deforming process of the sheet. To approach the stress state of the sheet in complex forming tools, the sheet is deformed to the same shape using the loading models shown in Fig. 2c and d. Because the loaded shapes in Fig. 2c and d are the same as in Fig. 2a, the same centre point O_α and curvature radius R_α are used for the two loading models. In Fig. 2c, L is the distance between the two supporting points. L_1 is the distance between the supporting point and the loading point with exerted loads of F''_1. d_{ll} is the loading displacement of the loading points to reach designed loaded shape. In Fig. 2d, q''_{load} is the line

load and d_{lm} is the displacement of the midpoint. The geometrical relation between loading point displacement d_{ll} and R_α can be obtained as:

$$R_a^2 = \left(L/2 - L_1\right)^2 + \left(\sqrt{R_a^2 - (L/2)^2} + d_{ll}\right)^2 \tag{3}$$

For centre point displacement d_{lm} and R_a, the geometric relation can be expressed as:

$$R_a = \sqrt{R_a^2 - (L/2)^2} + d_{lm} \tag{4}$$

And the relation between θ_a and R_a can be derived as:

$$\theta_a = 2\arctan\left((L/2)/\sqrt{R_a^2 - (L/2)^2}\right) \tag{5}$$

Hence, R_a and θ_a can both be determined with displacement d_{ll} or d_{lm}.

2.2 Strain and stress determination in loading stage

In loading stage, depending on the displacement exerted to achieve the target shape, the process can range from elastic to plastic loading. By dividing the initial undeformed sheet into equivalent m segments, Fig. 3a shows one of the sheet elements, defined as $a_0b_0c_0d_0$. Within elastic loading, the sheet element $a_0b_0c_0d_0$ is deformed to the shape $a_1b_1c_1d_1$. k_1 is defined as the deflection curvature and O_1 is the centre point of k_1. A polar coordinate system (r, θ) with the origin at the centre point O_1 is used to express the location of the sheet layers along thickness direction. As shown in Fig. 3a, θ_1 is the centre angle of $a_1b_1c_1d_1$. R_{n1} is the distance of the neutral plane to the centre point O_1 in elastic loading state, which can also be defined as the curvature radius in this state. Additionally, a local Cartesian coordinate system

Fig. 3 Schematic of deforming process in elastic loading and stress distribution through thickness. The labels in bracket in **b** are for the condition at the end of elastic loading

(a) Elastic deforming

(b) Stress distribution
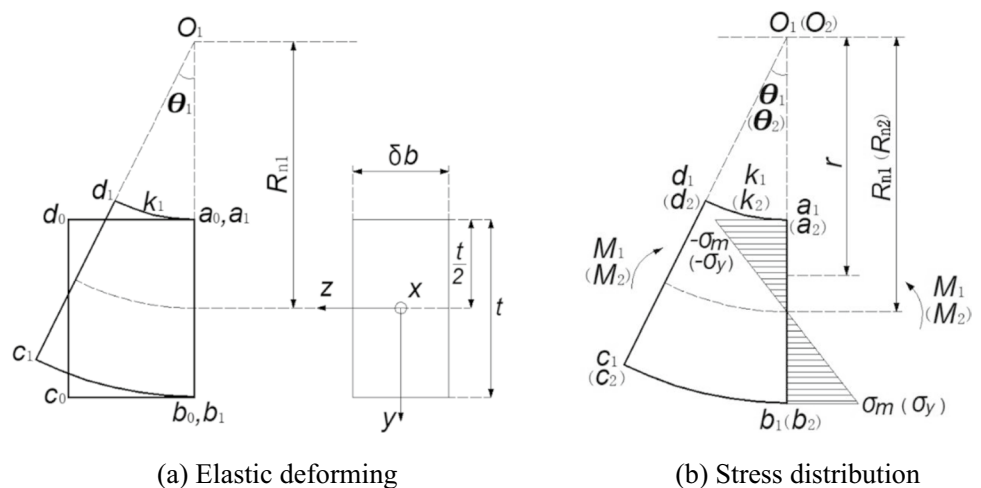
(x, y, z) is established to depict the plane perpendicular to the neutral plane of the sheet, in which y- and z-axes form the plane perpendicular to the deflection curvature and the neutral plane, and x axis locates at centroid of yz plane and is parallel to the neutral plane, as shown in the right half of Fig. 3a. Based on the assumption of Euler–Bernoulli beam theory, the neutral axis and neutral plane pass the centroid of yz plane as the mid layer of the sheet and no strain is generated at neutral plane. δb is the unit width of the sheet segment and is defined as 1 mm in this study. t is the sheet thickness.

When loading begins as exerting downward displacements on the sheet, elastic strain and stress are generated along x-axis direction in yz plane. The relation of deflection and induced moment depends on different loading model. For four-point loading model demonstrated in Fig. 2c, by utilising the Euler–Bernoulli beam theory, the relation between the loading point displacement d_{ll} and the generated moment M_1 in yz plane (Fig. 3b) in elastic loading can be expressed as [31]:

$$d_{ll} = \frac{M_1}{6EI}(3L_1L - 4L_1^2) \tag{6}$$

where E is the Young's modulus and I is the moment inertia of yz plane for z-axis. For uniform stress loading case demonstrated in Fig. 2d, the relation between the midpoint loading displacement d_{lm} and the moment M_1 in elastic loading is derived as [32]:

$$d_{lm} = \frac{40M_1L^2}{384EI} \tag{7}$$

Within linear elastic state, the distribution of stress in x direction along the thickness in yz plane is shown in Fig. 3b. In the figure, r is the distance of a random layer to the centre

point O_1, $-\sigma_m$ and σ_m are respectively the maximum compressive and tensile stresses achieved at the top and bottom surface of the sheet. The stress distribution can be expressed as:

$$\sigma = \frac{M_1}{I}\left(r - R_{n1}\right), \ R_{n1} - \frac{t}{2} \leq r \leq R_{n1} + \frac{t}{2} \tag{8}$$

As demonstrated in Fig. 3b, in elastic loading, the stress follows linear distribution along thickness (y direction).

With continued increasing of deflection, the strain and stress in x direction increases. When the absolute value of $-\sigma_m$ and σ_m reaches the yield stress σ_y, the current stress state is defined as end of elastic loading state. As illustrated in Fig. 3b, the deformed sheet segment, curvature, centre point, centre angle, and moment at the end of elastic loading state are respectively defined as $a_2b_2c_2d_2$, k_2, O_2, θ_2, and M_2, and the distance of neutral plane to the centre point O_2 at the end of the state is defined as R_{n2}.

Further increase in deflection will lead to the stress surpassing the elastic region, i.e. reaching plastic region. Figure 4 shows the case after entering the plastic loading state. In the plastic loading state, the elastically loaded shape of sheet element $a_2b_2c_2d_2$ further deforms to $a_3b_3c_3d_3$, with deflection curvature increasing from k_2 to k_3 as shown in Fig. 4a. Simultaneously, the centre angle increases from θ_2 to θ_3, and the centre point and neutral plane respectively change from position O_2 to O_3 and R_{n2} to R_{n3} (R_{n3} is the distance of neutral plane to the centre point O_2 in plastic loading). In this situation, the linear elastic stress–strain relation is broken down in the outer bending layers, and plastic strain is generated in the plastic regions near the top and bottom surfaces of the sheet as shown in the red regions in Fig. 4b. The location of the transition boundary from elastic to plastic region near the top surface is defined using r_i as the distance to

Fig. 4 Schematic of deforming process from elastic to plastic loading state in CAF and stress distribution through the thickness of the sheet

(a) Schematic of deforming process

(b) Stress distribution
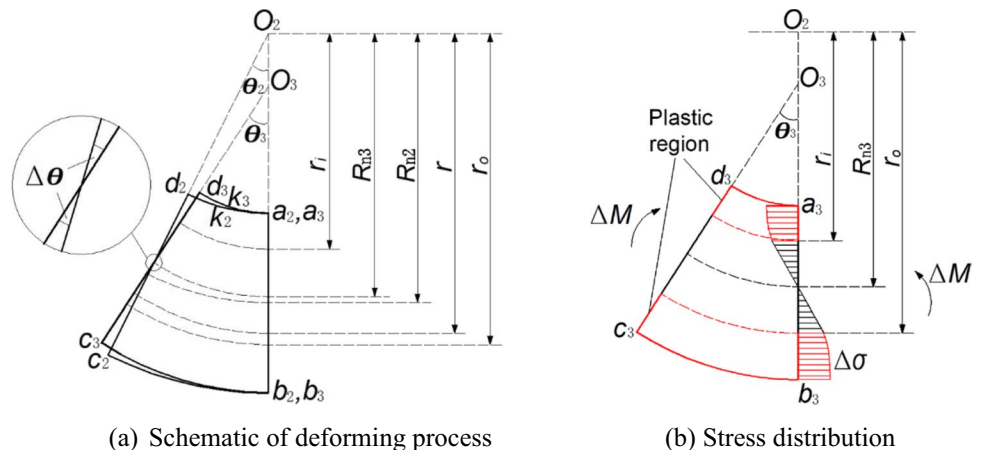
the centre point O_2, while r_o is used to mark the distance for the position of transition boundary near bottom. The layers above r_i and underneath r_o are the plastic regions. With the increase of deflection, the upper elastic–plastic boundary will move downwards, and the lower boundary will move upwards, i.e. r_i increases and r_o decreases. $\triangle\sigma$ and $\triangle M$ in Fig. 4b are respectively the increment of stress and corresponding moment in deformation from $a_2b_2c_2d_2$ to $a_3b_3c_3d_3$.

By applying the Winkler's theory, the strain generated at layer at position r when the element deforms from $a_2b_2c_2d_2$ to $a_3b_3c_3d_3$ can be expressed as:

$$\Delta\varepsilon = \frac{\Delta\theta(r - R_{n3})}{r\theta_2} \tag{9}$$

where $\Delta\varepsilon$ is the strain accumulated at layer of position r in the transformation process from $a_2b_2c_2d_2$ to $a_3b_3c_3d_3$, and $\triangle\theta$ is the change of centre angle as $\triangle\theta = \theta_3 - \theta_2$ as illustrated in Fig. 4a. From Eq. (9), zero strain increment was derived in the layer of neutral plane R_{n3}. When layer r locates underneath R_{n3}, i.e. $r > R_{n3}$, positive strain is generated and the layer in that position is in tension state. In contrast, when located above the neutral plane ($r < R_{n3}$), negative strain is induced as in compression state. When r is equivalent to r_i or r_o, the layer is at the transition boundary from elastic region to plastic region. According to the definition, the strain at elastic–plastic boundary at r_i and r_0 equals to:

$$\varepsilon_y = \begin{cases} -\frac{\sigma_y}{E}, & r = r_i \\ \frac{\sigma_y}{E}, & r = r_0 \end{cases} \tag{10}$$

where ε_y is the strain at yield stress σ_y at transition boundary r_i and r_0. Additionally, under the assumption that transverse shear strain is neglected in Winkler's theory, ε_y can be derived as comprised of two parts as:

$$\varepsilon_y = \varepsilon_2' + \Delta\varepsilon' \tag{11}$$

where ε_2' is the strain generated at the same layer at r_i or r_0 when the sheet is loaded to the end of elastic loading state. $\Delta\varepsilon'$ is the accumulated strain at r_i or r_0 during deformation from the end of elastic loading $a_2b_2c_2d_2$ to $a_3b_3c_3d_3$ in plastic loading state. By utilising the linear stress–strain relation shown in Fig. 3b and applying Eqs. (10) and (11), ε_y can be further expressed as:

$$\begin{cases} \varepsilon_2' = \varepsilon_y\left(\frac{r-R_{n2}}{t/2}\right) \\ \Delta\varepsilon' = \frac{\Delta\theta(r-R_{n3})}{r\theta_2} \\ \varepsilon_y = \varepsilon_2' + \Delta\varepsilon' \end{cases}, r = r_i \text{ or } r = r_0 \tag{12}$$

Due to the linear relation for strain and stress within elastic region, Eq. (12) can be further extended to describe the elastic strain ε_e and stress σ_e at random position r within elastic region ($r_i \leq r \leq r_0$) when deforms to $a_3b_3c_3d_3$ as:

$$\begin{cases} \varepsilon_2'' = \varepsilon_y\left(\frac{r-R_{n2}}{t/2}\right) \\ \Delta\varepsilon'' = \frac{\Delta\theta(r-R_{n3})}{r\theta_2} \\ \varepsilon_e = \varepsilon_2'' + \Delta\varepsilon'' \\ \sigma_e = E\varepsilon_e \end{cases}, r_i \leq r \leq r_0 \tag{13}$$

where ε_2'' is the strain generated at position r in elastic region ($r_i \leq r \leq r_0$) when deforms to $a_2b_2c_2d_2$ as the end of elastic loading. $\Delta\varepsilon''$ is the accumulated strain at r in plastic loading state from $a_2b_2c_2d_2$ to $a_3b_3c_3d_3$. ε_e and σ_e are respectively the strain and stress at position r in linear elastic region of $a_3b_3c_3d_3$.

As shown in Fig. 4b, plastic strain is induced in the layers located above r_i and below r_0. To reflect the relation between plastic strain and flow stress beyond linear elastic relation in the plastic region, the classical power law function was used to express work hardening behaviour of the material as:

$$\sigma_p = \sigma_y + h\varepsilon_p^n \tag{14}$$

where σ_p is defined as the flow stress in the plastic region. σ_y is the yield stress of material and ε_p is the plastic strain. h and n are material constants. By combining Eqs. (9) and (14), the flow stress at specific layer r in plastic region can be expressed as:

$$\sigma_p = \sigma_y + h\left(\frac{\Delta\theta(r - R_{n3})}{r\theta_2}\right)^n, \quad r < r_i \text{ or } r > r_0 \tag{15}$$

In the yz plane of the sheet, the force equilibrium function can be derived as:

$$\int \sigma \, dA = 0 \tag{16}$$

where A is the area of the yz plane of the sheet. With further transformation of $dA = \delta b dy = dy = d(r - R_{n2}) = dr$, the equation can be written as:

$$\int_{R_{n2}-t/2}^{R_{n2}+t/2} \sigma dr = \int_{r_i}^{r_0} \sigma_e dr + \int_{r_i}^{R_{n2}-t/2} \sigma_p dr + \int_{r_0}^{R_{n2}+t/2} \sigma_p dr = 0 \tag{17}$$

By inserting Eqs. (13) and (15) into Eq. (17), Eq. (17) can be expressed in a function which R_{n3} is the only parameter as:

$$f(R_{n3}) = 0 \tag{18}$$

Detailed function derivation process is given in Appendix 1. With the determination of R_{n3}, by adopting Eqs. (13) and (15), the strain and stress in both elastic and plastic regions can be determined. Hence the moment in yz plane

around z axis for $a_3b_3c_3d_3$, defined as M_3, can be derived as:

$$M_3 = M_2 + \Delta M = \int \sigma(r - R_{n2})dA \qquad (19)$$

where M_2 is the moment at $a_2b_2c_2d_2$ and $\triangle M$ is the moment increased during the deformation from $a_2b_2c_2d_2$ to $a_3b_3c_3d_3$ as respectively shown in Figs. 3b and 4b.

2.3 Springback prediction after creep-ageing

In creep-ageing stage, stress relaxation will be induced due to accumulation of the creep strain. For layer at location r in the deformed element with elastic loading $a_1b_1c_1d_1$ or plastic loading $a_3b_3c_3d_3$, the stress variation in creep-ageing stage in respect of ageing time t_a can be expressed as:

$$\sigma(t_a) = \sigma - \sigma_r(t_a) = \sigma - E\varepsilon_c(t_a) \qquad (20)$$

where $\sigma(t_a)$ is the stress at ageing time t_a of the layer, σ is the stress generated at the end of loading stage. $\sigma_r(t_a)$ is the extent of stress relaxation at ageing time t_a due to generation of creep strain, which can be calculated as $\sigma_r(t_a) = E\varepsilon_c(t_a)$ where $\varepsilon_c(t_a)$ is the creep strain accumulated at layer r at ageing time t_a. It is also known that the evolution of creep strain is determined by the stress in creep-ageing, by applying proper constitutive model reflecting the relation of stress and creep strain, $\varepsilon_c(t_a)$ can be obtained as:

$$\varepsilon_c(t_a) = f_c(\sigma(t_a)) \qquad (21)$$

f_c denotes the constitutive model being used. The creep strain accumulated after completion of creep-ageing at time of t_{end} is denoted as $\varepsilon_c(t_{end})$.

In unloading stage, with the upward movement of the loading points and decrease of d_l and d_{lm}, driven by the recovery of remaining elastic strain after creep-ageing, springback of the deformed sheet is induced. The springback of the sheet will stop when recovery of elastic strain is completed. Hence, the strain and stress in springback follows linear elastic relationship and the unloading process can be viewed as a reversed process of elastic loading. The strain distribution along the thickness of the sheet at the end of creep-ageing in elastic/plastic loading state is demonstrated in Fig. 5.

As shown in Fig. 5, after completion of creep-ageing, the remaining elastic strain $\varepsilon_e(d)$ at specific layer d of the sheet, along with the induced moment M_{end} for yz plane around z axis as the recovery moment at the end of creep-ageing/start of unloading stage, can be expressed as:

$$\begin{cases} \varepsilon_e(d) = \varepsilon(d) - \varepsilon_p(d) - \varepsilon_c(t_{end}) \\ M_{end} = \int E\varepsilon_e(d)y_d dA \end{cases} \qquad (22)$$

where $\varepsilon(d)$, $\varepsilon_p(d)$, and $\varepsilon_c(t_{end})$ are respectively the strain, plastic strain, and creep strain in x direction at layer d of the sheet, and y_d is the distance of the layer to the neutral plane. For four-point bending cases, by applying Eq. (6), the recovered deflection at loading point (d_{rl}) during springback can be obtained as $d_{rl} = \frac{M_{end}}{6EI}(3L_1L - 4L_1^2)$. For uniform stress bending cases, by applying Eq. (7), the recovered deflection at midpoint of the sheet (d_{rm}) can be derived as $d_{rm} = \frac{40M_{end}L^2}{384EI}$. By utilising Eqs. (3) and (4) respectively for four-point bending and uniform stress bending cases, the curvature $1/R_b$, as the final curvature of CAFed sheet, can be derived as $R_b^2 = (L/2 - L_1)^2 + \left(\sqrt{R_b^2 - (L/2)^2} + (d_{ll} - d_{rl})\right)^2$ for the former case and $R_b = \sqrt{R_b^2 - (L/2)^2} + (d_{lm} - d_{rm})$
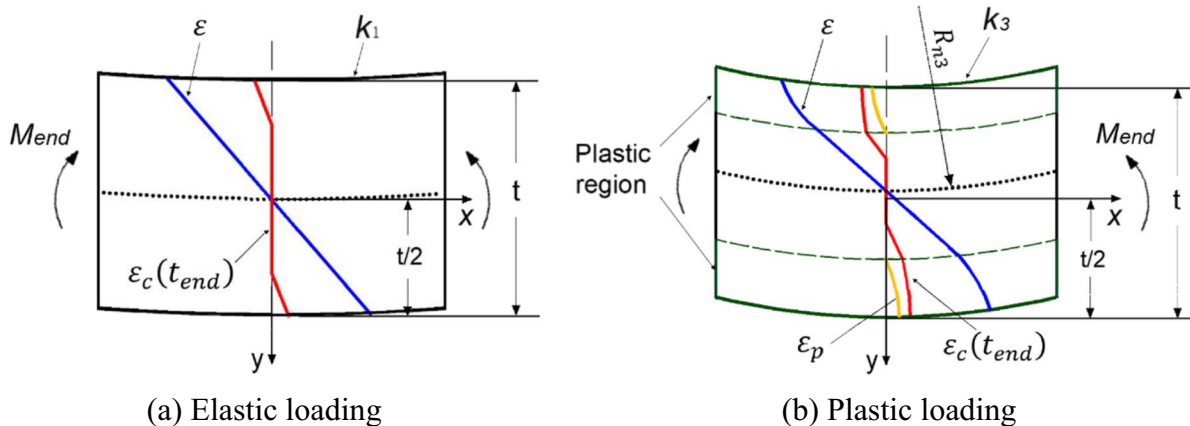

(a) Elastic loading

(b) Plastic loading

Fig. 5 Schematic of strain (x direction) distribution along thickness of the sheet (y direction) after completion of creep-ageing. ε is the bending strain in x direction. The dotted lines stand for neutral plane of the sheet

for the latter. By applying geometric transformation derived in Eq. (4), the final deflection of the sheet at the midpoint can be expressed as:

$$\Delta d_f = R_b - \sqrt{R_b^2 - (L/2)^2} \qquad (23)$$

3 Springback compensation method based on closed-form solution

The above closed-form solution of springback prediction for CAF is based on two simplified loading models, i.e. four-point bending and uniform stress bending. In practical CAF fabrication, however, specialised forming tool may be used, in which a higher complexity of loading state for the forming sheet is involved. Multipoint flexible tool, as one of the state-of-the-art forming tools, is characterised by its flexibility in setting required loading shape and has been adopted to not only CAF but also other sheet forming processes [5, 22, 33]. When deforming with flexible tool, depending on the designed loaded shape, the loading process can span from linear elastic to nonlinear plastic loading. For elastic loading with a multipoint flexible tool, the loading state is varying with the increase of loading displacement, which can be difficult to analytically derive the relation between loading deflection and stress states of the forming sheet. Furthermore, the derived solution will lose its validity once the locations of loading points are modified. By applying the simplified uniform stress bending model and Eq. (7), when the sheet is deformed in elastic loading with flexible tool, an equation with higher convenience and robustness to express the relation between loading displacement d_{lm}' and induced moment M_1 is proposed as:

$$d_{lm}' = \alpha' \frac{40 M_1 L^2}{384 EI} \qquad (24)$$

where d_{lm}' is the displacement at midpoint of the sheet adopting flexible tool, and a' is the adjustment factor to approach real relation between generated moment and d_{lm}' within elastic loading. When d_{lm}' continues to increase and reach the end of elastic loading state, Eq. (24) can be further written as $d_{lm}' = \alpha' 40 M_2 L^2 / 384 EI$, where M_2 is the moment induced at the end of elastic loading as illustrated in Fig. 3b.

When the stress surpasses elastic region during loading, as shown in Eq. (9), the strain increment $\triangle \epsilon$ in plastic loading state is derived based on geometrical change with the increase in deflection from the end of elastic loading. Consequently, the proposed solution for stress analysis and springback prediction in plastic loading state (from Eqs. (9) to (23)) remains its validity in the case of

multipoint flexible forming tool. Hence, by replacing Eqs. (7) with (24), a modified closed-form springback prediction solution (Eqs. (8) to (24)) is obtained for multipoint flexible tool. As can be noticed, the accuracy of this modified springback prediction solution for CAF with flexible tool is highly depending on the determination of adjustment factor a'. This adjustment factor not only helps to approach true relation of deflection and the generated moment within elastic loading, but also defines the transformation boundary from elastic to plastic loading. The solution-based springback compensation method, aiming at forming sheet with target curvature by approaching appropriate adjustment factor α' through iterations, can be generalised as follows:

(1) With a determined target curvature as $1/R_c$ and adjustment factor α_i', the loaded shape with curvature as $1/R_a^i$ for i^{th} iteration CAF can be derived based on the modified closed-form springback prediction solution (Eqs. (8) to (24)). For the first iteration, the initial adjustment factor α_i' is set to be 1.

(2) The ith iteration CAF is conducted with flexible forming tool which is adjusted to the derived loaded curvature $1/R_a^i$. After completion of CAF, curvature of the CAFed sheet in that iteration is obtained and denoted as $1/R_b^i$. R_b^i is then compared with the target curvature radius . Δe is the shape error at midpoint between the CAFed and target shape and can be obtained by using Eq. (23) as $\Delta e = \left(R_c - \sqrt{R_c^2 - (L/2)^2} \right) - \left(R_b^i - \sqrt{R_b^{i\,2} - (L/2)^2} \right)$.

(3) If the absolute value of shape error $|\Delta e|$ exceeds the tolerance range Tol_1, with the obtained CAFed curvature $1/R_b^i$ in i^{th} iteration, the adjustment factor α_{i+1}' for next $(i + 1)^{th}$ iteration is updated based on the modified closed-form springback prediction solution (Eqs. (8) to (24)). With the updated adjustment factor, the next iteration is started from step (1).
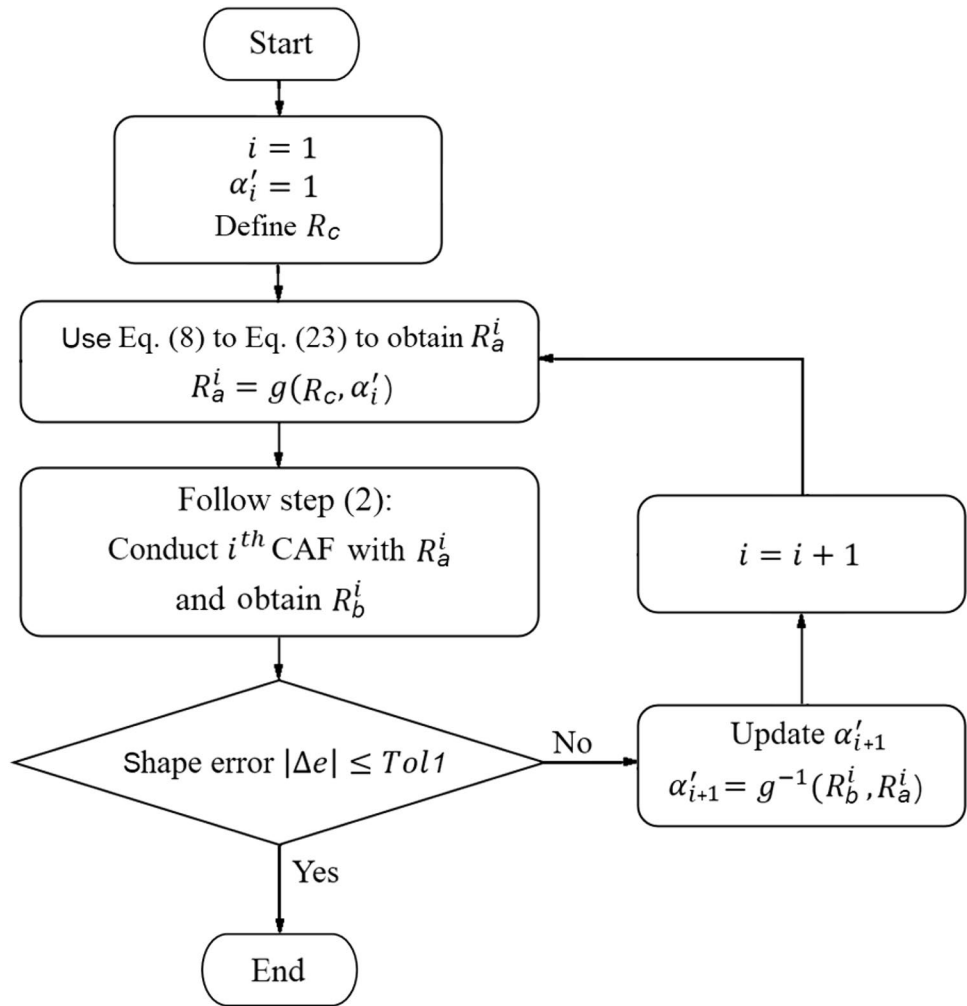
A flowchart of the proposed closed-form solution-based springback compensation method is demonstrated in Fig. 6, where i stands for the ith iteration with the method and function g stands for the modified springback prediction solution (Eqs. (8) to (24)).

4 Experimental procedure

4.1 Material

The material used was a 3rd generation Al-Li alloy with major compositions of 0.6–0.9 wt% Li, 3.4–4.5 wt% Cu, and 0.6–1.1 wt% Mg. The as-received material was in the

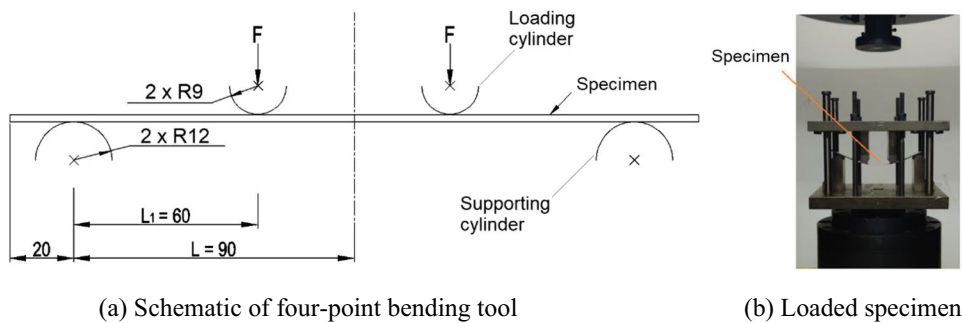**Fig. 6** Flowchart of closed-form solution-based springback compensation method

```
                          Start
                            │
                            ▼
                        i = 1
                       α'ᵢ = 1
                      Define R_c
                            │
                            ▼
        Use Eq. (8) to Eq. (23) to obtain Rₐⁱ  ◄──────────┐
                 Rₐⁱ = g(R_c, α'ᵢ)                          │
                            │                               │
                            ▼                               │
                 Follow step (2):                      i = i + 1
              Conduct iᵗʰ CAF with Rₐⁱ                      ▲
                  and obtain R_bⁱ                           │
                            │                               │
                            ▼                    No    Update α'ᵢ₊₁
        Shape error |Δe| ≤ Tol1  ─────────────────►  α'ᵢ₊₁ = g⁻¹(R_bⁱ, Rₐⁱ)
                            │
                           Yes
                            │
                            ▼
                          End
```

$$Rₐⁱ = g(R_c, α'_i)$$
$$α'_{i+1} = g^{-1}(R_b^i, R_a^i)$$
Shape error $|Δe| ≤ Tol1$

Table 1 Material constants for the Al-Li alloy

E	h	n	σ_y(0.1% offset)
69.8 GPa	91	0.53	453 MPa

form of sheets with 2, 4, and 6 mm thickness in T8 temper which is the commonly adopted finish temper for the 3rd generation Al-Li alloys [27]. The material constants for this Al-Li alloy are listed in Table 1, where h and n are the constants used in Eq. (14). The adopted creep-ageing constitutive model f_c is presented in Appendix 2.

Fig. 7 Schematic of four-point bending tool (dimensions in mm) and photo with loaded specimen

2 x R9
2 x R12
$L_1 = 60$
$L = 90$
20
F
F
Loading cylinder
Specimen
Supporting cylinder
Specimen

(a) Schematic of four-point bending tool   (b) Loaded specimen

Table 2 Four-point bending CAF experiments in elastic loading, with the same maximum loading surface stress of 430 MPa

Thickness (mm)	Designed loading displacement d_{ll} (mm)	Loading force F (N)	Maximum stress (MPa)
2	18.7	103.0	430
4	9.2	420.4	430
6	5.9	1036.4	430

Table 3 Four-point bending CAF experiments with the same targeted curvature

Thickness (mm)	Designed loading displacement d_{ll} (mm)	Target curvature (mm^{-1})	Target Δd_f (mm)
2	20.2	1/2000	2.03
4	10.8	1/2000	2.03
6	7.3	1/2000	2.03

4.2 Four-point bending CAF experiments

Four-point bending tests were conducted to verify the established closed-form springback prediction solution. Strip shape specimens with dimension of 220 mm × 20 mm and thickness of 2, 4, and 6 mm were adopted in the testes. The four-point bending tool is composed of two upper loading cylinders and two supporting cylinders as shown in Fig. 7. The specimen was placed on the two supporting cylinders of the four-point bending tool with dimension as illustrated in Fig. 7. The specimens were deformed with designed loading displacement d_{ll} covering both elastic and plastic loading by the loading cylinders which are then fixed during

creep age forming at 143 °C for 5 h. After completion of the creep-ageing, the specimen was cooled down in the air to room temperature with the bending tool and unloaded to allow happening of springback to obtain the final deformed curvature. The test groups for CAF under constant maximum surface stress of 430 MPa in elastic loading and with constant target curvature are listed in Tables 2 and 3 respectively. In Table 2, the specimens of different thicknesses were loaded with different displacements to reach the same maximum surface stress of 430 MPa within elastic region of the material. In Table 3, different loading displacements were adopted to creep age forming specimens with the same target curvature of 1/2000 mm^{-1}.

Fig. 8 Multipoint flexible tool and its dimensions

(a) Flexible tool with loaded specimen

(b) Setup of specimen with the tool

(c) Geometry and pin arrangements (dimension in mm).
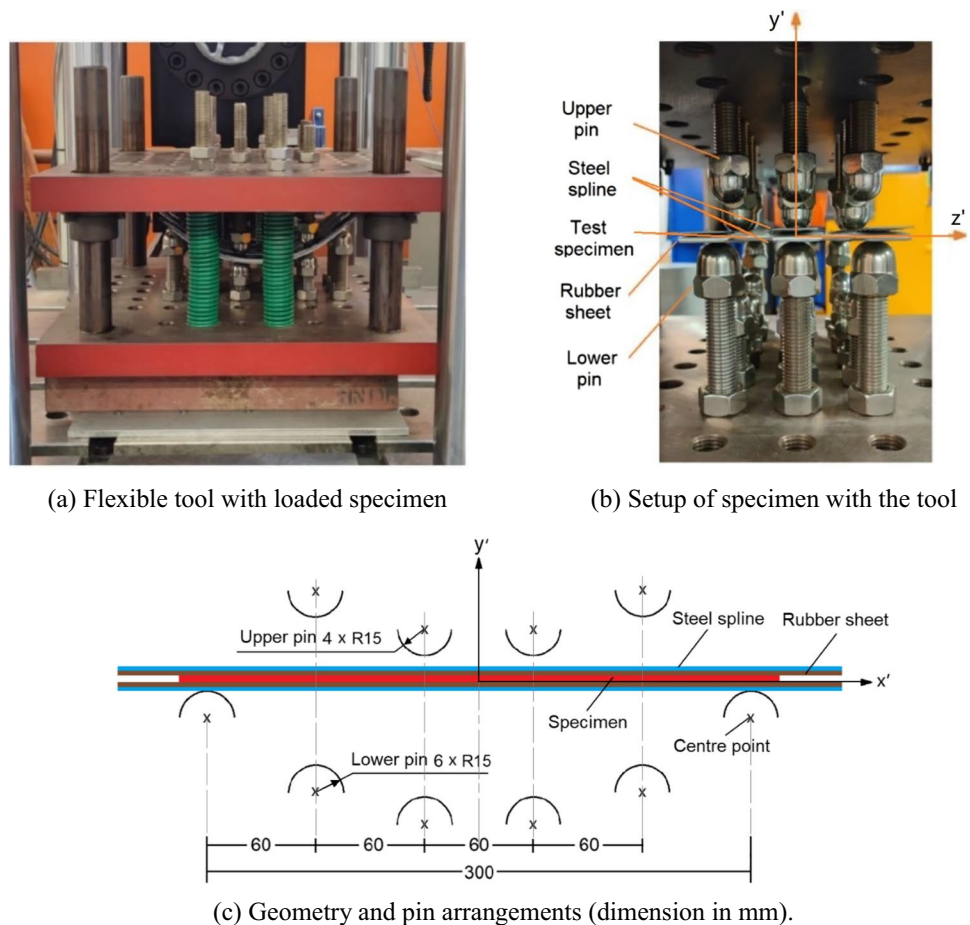
4.3 Flexible tool CAF experiments

Specimens of the same material were used in the tests to verify the proposed springback compensation method for CAF. The specimen dimensions were 335 mm × 165 mm for 2 mm sheets, and 320 mm × 165 mm for 4 mm sheets. A flexible tool as shown in Fig. 8a was employed. The setup, dimension and pin arrangements are illustrated in Fig. 8b and c. *x', y'* and *z'* are the axes parallel to the specimen's length, thickness, and width directions, and the origin of the coordinate system *x'y'z'* locates at the centre point of the specimen bottom surface as shown in Fig. 8c. A 3 (rows) × 6 (columns) pin matrix was adopted for lower pins and a 3 (rows) × 4 (columns) matrix for the upper pins. To achieve more evenly distributed pressure applied on the specimen, for each row of pins, two steel splines with a dimension of 400 mm × 30 mm and 1.2 mm thickness were placed on the top and bottom of the specimen, aligned with the pin row. Rubber sheets were used between the upper and lower splines and the specimen to eliminate/minimise any damage to the specimen, as shown in Fig. 8b. The centre line interval for each two-neighbouring upper/lower pins in all rows (*x'* direction) and columns (*y'* direction) is 60 mm. The heights of the pins in each column were adjusted to be consistent with the designed loading curvature of the specimen. The same target curvature of 1/2000 mm^{-1} was set for CAF fabrication with flexible tool as shown in Table 4. In each iteration, the specimen was deformed to the loaded curvature $1/R_a^1$ and then fixed for creep-ageing at 143 °C for 5 h. After completion of the creep-ageing, the specimen was cooled down in the air with the flexible tool to room temperature and unloaded to obtain the final deformed curvature after springback. For verification purpose, the error tolerance Tol_1 of absolute shape error |Δ*e*| was set to be 1/10 of the target Δd_f as 0.56 mm.

5 Results and discussions

5.1 Four-point bending CAF experiments

Figure 9 shows the springback results for all thicknesses, including the prediction curves of the midpoint loading deflection $\underline{d}_{lm}$ with the final deflection Δd_f at the same

Table 4 Experiment programme for CAF of target curvature with flexible tool

Thickness (mm)	Target curvature (mm^{-1})	Target Δd_f (mm)
2	1/2000	5.63
4	1/2000	5.63

midpoint of the CAFed specimen, and the moment release curves in creep-ageing for the moment at the end of creep-ageing stage M_{end} as a function of the moment at the end of loading stage M_{load} The evolutions of maximum absolute values of creep strain $\varepsilon_c(t_{end})$ and plastic strain ε_p at the end of creep-ageing, which were obtained at upper surface layer of the sheet, are also demonstrated with the increase of M_{load} in the figure. These results (solid lines) were obtained using the closed-form solution proposed in this study. For comparison, the dotted lines are the prediction results derived from the traditional beam theory with assumption of small deflection as [20]:
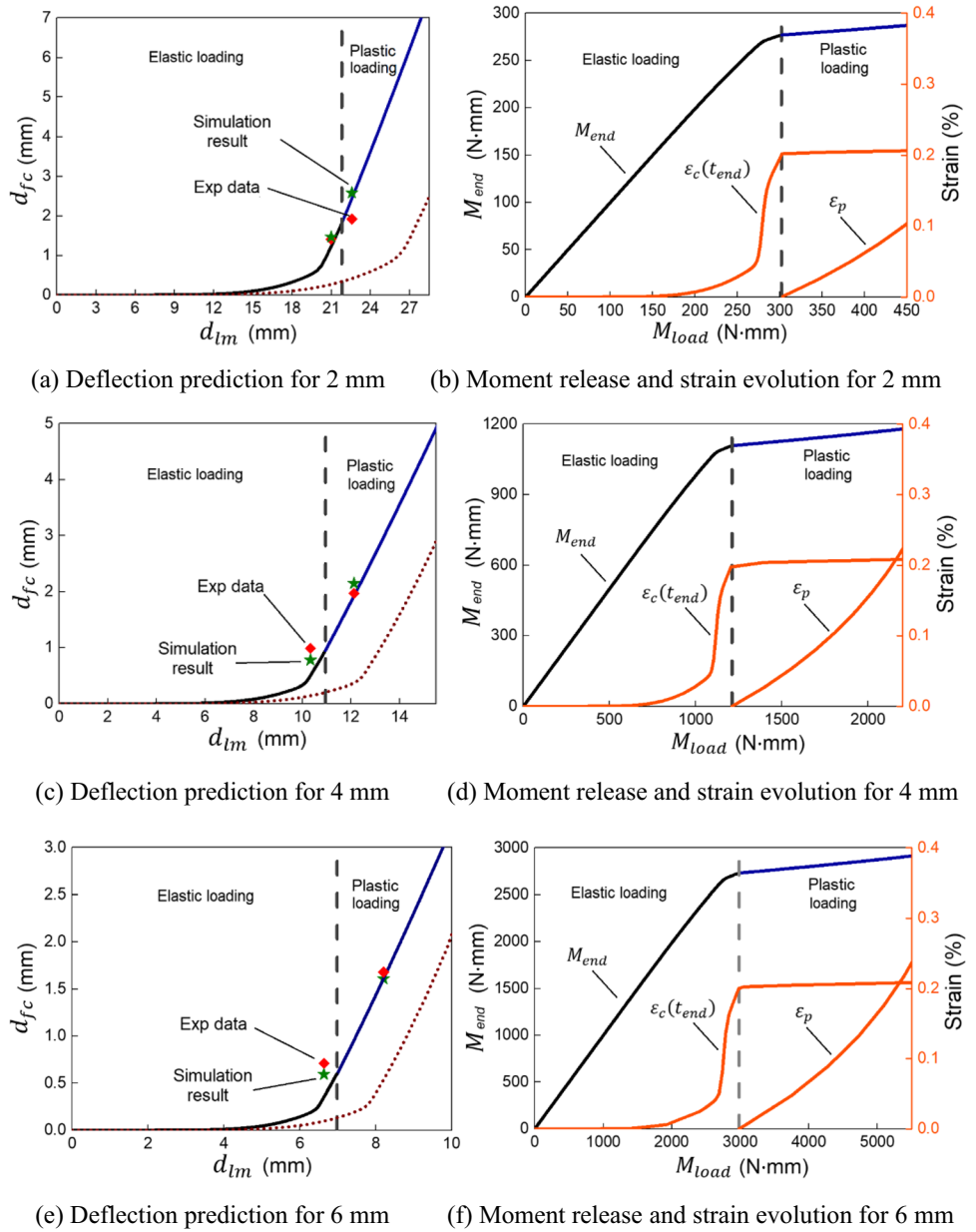
$$\begin{cases} \varepsilon(d) = k_b y_d, & -t/2 \le y_d \le t/2 \\ \sigma(d) = E\varepsilon(d), & -\sigma_y/(Ek_b) \le y_d \le \sigma_y/(Ek_b) \\ \sigma(d) = \sigma_y + h(\varepsilon(d) + \sigma_y/E)^n, & \sigma_y/(Ek_b) \le y_d \le t/2 \\ \sigma(d) = \sigma_y + h(\varepsilon(d) - \sigma_y/E)^n, & -t/2 \le y_d \le -\sigma_y/(Ek_b) \end{cases} \quad (25)$$

where k_b is the loaded curvature as $1/R_b$, $\sigma(d)$ is the corresponding induced stress at layer d. The experimental data and numerical simulation results are also presented using diamond and star shape symbols respectively. The FE model for obtaining the presented data is presented in Appendix 3. In addition, the comparisons of all obtained results of springback percentage (*sp*) in the two test groups with different thicknesses, calculated using $sp = (1 - \Delta d_f/d_{lm}) \times 100\%$, are demonstrated in Fig. 10.

As demonstrated in Figs. 9 and 10, for all thicknesses, satisfactory convergences were achieved among results of the solution-based predication, four-point bending CAF experiments, and numerical simulation, indicating validity of the proposed closed-form solution. The predicted springback results by the solution have a maximum difference of 0.49 mm from the experiments and 0.27 mm from the FE simulations, while the beam theory-based results have much larger deviations, especially in the plastic loading region, with a maximum prediction error of 1.6 mm for the 4 mm thickness sheet. In addition, by comparing the obtained prediction curves of the beam theory-based and the solution-based solutions respectively in Fig. 9a, c, and e, a similar trend which can be identified for all thicknesses is that with the same loading displacement d_{lm}, the prediction result d_{fc} for the beam theory-based method is always lower than the solution-based method, indicating that a lower stress is calculated by the former method than the latter.

In addition, based on the obtained prediction curves, different evolution trend can be observed in elastic and plastic loading conditions for all thicknesses as shown in Fig. 9. In elastic loading, the CAFed deflection Δd_f and moment release (M_{load}–M_{end}) gradually increased at the beginning and surged with higher rate when approaching the plastic loading. In plastic loading, a high increase rate of Δd_f and (M_{load}–M_{end}) were obtained for all thicknesses. On the other

Fig. 9 Creep age forming behaviour for 2, 4, and 6 mm sheets, showing the predicted, FE simulated, and experimental final deflection Δd_f vs loading displacement d_{lm}; the moment M_{end}, strain ε_c, and plastic strain ε_p at the end of creep-ageing as a function of loading moment M_{load}

(a) Deflection prediction for 2 mm

(b) Moment release and strain evolution for 2 mm

(c) Deflection prediction for 4 mm

(d) Moment release and strain evolution for 4 mm

(e) Deflection prediction for 6 mm

(f) Moment release and strain evolution for 6 mm

Fig. 10 Comparison of the springback percentage results in two test groups with different thicknesses. The legends from left to right respectively stand for results of experiment, numerical simulation, closed-form solution, and the beam theory-based solution

(a) Test group of elastic loading

(b) Test group of constant curvature
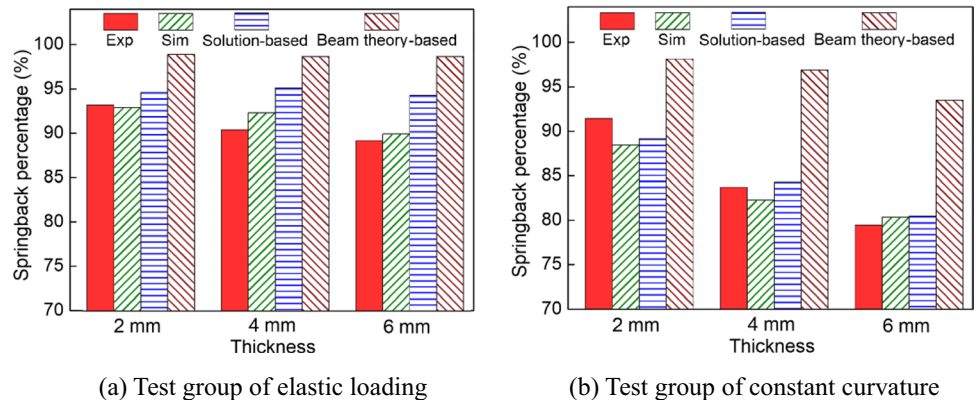
Fig. 11 Photos of CAF iteration results of sheets with different thickness

(a) 2 mm

(b) 4 mm
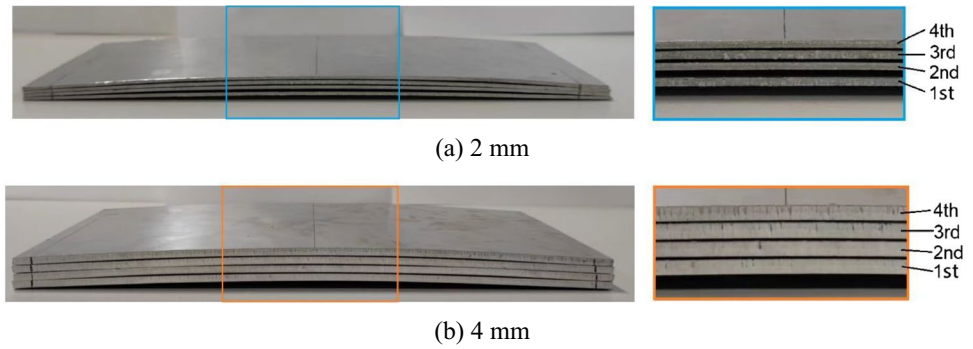
Fig. 12 Comparison of the 4th iteration loaded curvature $1/R_a^4$, CAFed curvature $1/R_b^4$, FE simulated result $1/R_s^4$, and target curvature $1/R_c$, $R_c = 2000$ mm, for 2 mm and 4 mm sheets. The dot symbols are measured points at corresponding positions of x' axis

(a) 2 mm

(b) 4 mm
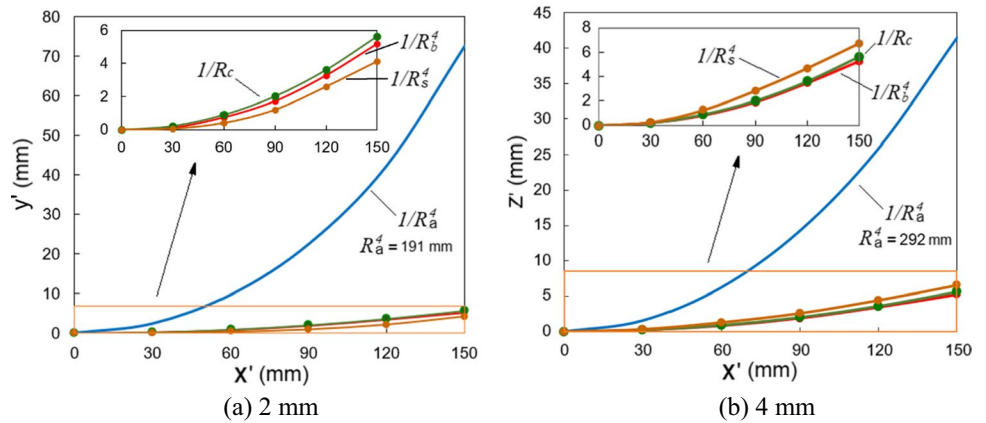
hand, as demonstrated in Fig. 9b, d, and f, the final creep strain surged when approaching plastic loading state and maintained at a level slightly above 0.2% with minor increase in plastic loading, while the plastic strain during loading increased sharply with increasing moment. The observed surge for deflection Δd_f, moment release (M_{load}–M_{end}), and maximum creep strain when approaching plastic loading can be attributed to the nonlinear increase of creep deformation of the alloy when the applied stress surpasses 400 MPa, which was observed in uniaxial creep-ageing tests at 143 °C for this material [29]. The high increase rate of Δd_f and

(M_{load}–M_{end}) achieved in plastic loading is due to the effects of plastic strain and larger creep strain respectively induced in stages of loading and creep-ageing. Additionally, for this Al-Li alloy, springback is high and can offset the majority of the loading displacement. As demonstrated in Fig. 10, the lowest springback percentage is 79.5% for 6 mm sheet for CAF of a target curvature of 1/2000 mm^{-1}. It can be noted that due to high strength and creep resistance of the alloy, even for fabricating panels with a small curvature of 1/2000 mm^{-1}, CAF need be conducted with plastic loading state.

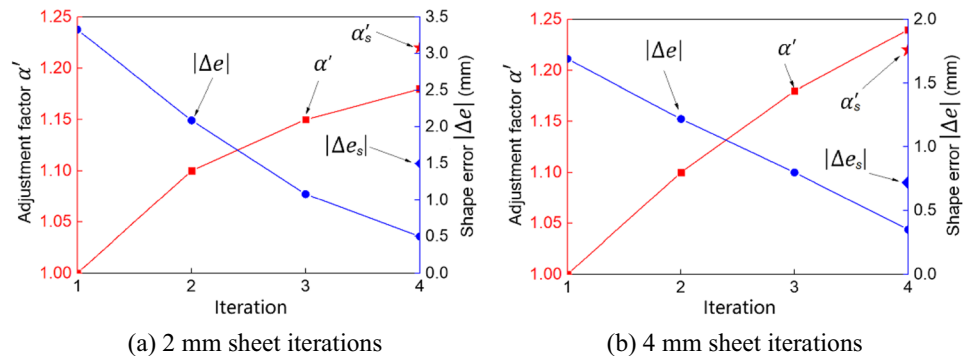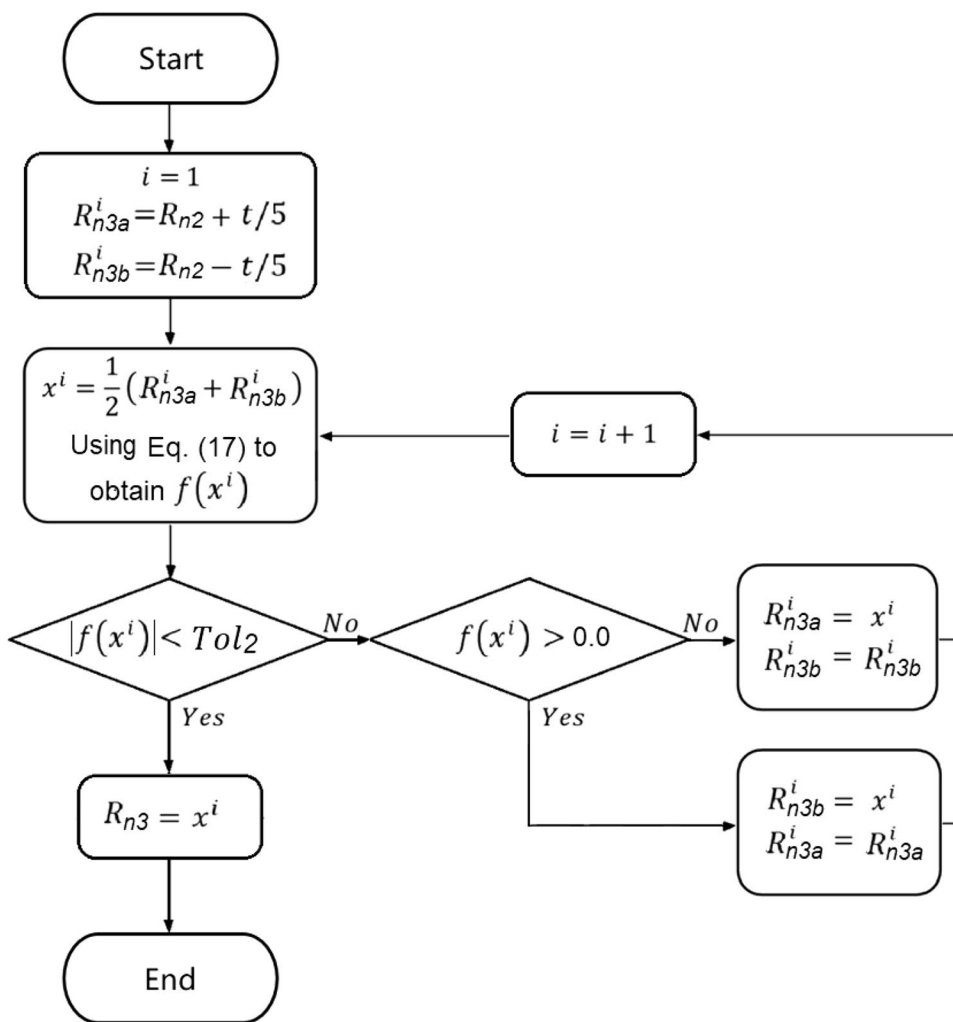**Fig. 13** Evolution of adjustment factor and shape error with increased iterations

(a) 2 mm sheet iterations

(b) 4 mm sheet iterations

Fig. 14 Flowchart of bisection method

5.2 Flexible tool CAF experiments

Figure 11 shows the photos of the CAFed sheets using the solution-based springback compensation method proposed in this study. As demonstrated in Fig. 11, the final deflection increases with increasing iteration for both 2 and 4 mm sheets. Within 4 iterations, the final error in the shape/curvature falls in the range of error tolerance Tol_1 of 0.56 mm. Figure 12 is the comparison of the curvatures for the target value with the loaded, CAFed, and FE simulated results in the final 4th iteration for 2 and 4 mm sheets. As shown in the figure, similar to the four-point bending tests, for CAF of $1/2000$ mm^{-1} curvature sheets using flexible tool, large loading displacement and high springback were observed. For 2 and 4 mm sheets, the maximum loading displacement

d_{lm} was respectively 12.9 and 7.4 times larger than the target deflection Δd_f, with a springback percentage of 92.9% and 87.4%.

Figure 13 presents the evolution of adjustment factor α' and shape error $|\triangle e|$ with increasing iterations, together with the FE simulation results of adjustment factor (α'_s) and shape error ($|\triangle e_s|$) based on the loaded shape of 4th iteration. As shown in the figure, for 2 and 4 mm sheets,

Table 6 Material constants for the constitutive equations [34]

A_1(h^{-1})	A_2(MPa)	A_3(h^{-1})	B	B_1(MPa^{-1})	C_p
26	14	8.43E-8	10.5	3.6E-2	6.5E-3
C_r(h^{-1})	E' (MPa)	K	k'_1	k'_2	m_1
8E-2	6.26E4	9.36E-8	0.5	5.2E-2	5.42E-1
m_{1a}	m_2	m_3	m_4	n'	n_{1a}
0.52	0.75	1.05	1.5	2.35	50
n_2	Q	γ_0	σ_{end}(MPa)		
1.28	1.52	8	396		

Table 5 Initial values for the constitutive equations [34]

$\overline{\rho}_0$	$\overline{r}$	ε'_p	σ_{th0}(MPa)
0	1	0	105

Fig. 15 Schematic of the FE model for four-point bending. Dimensions in mm. 'RP' stands for reference point
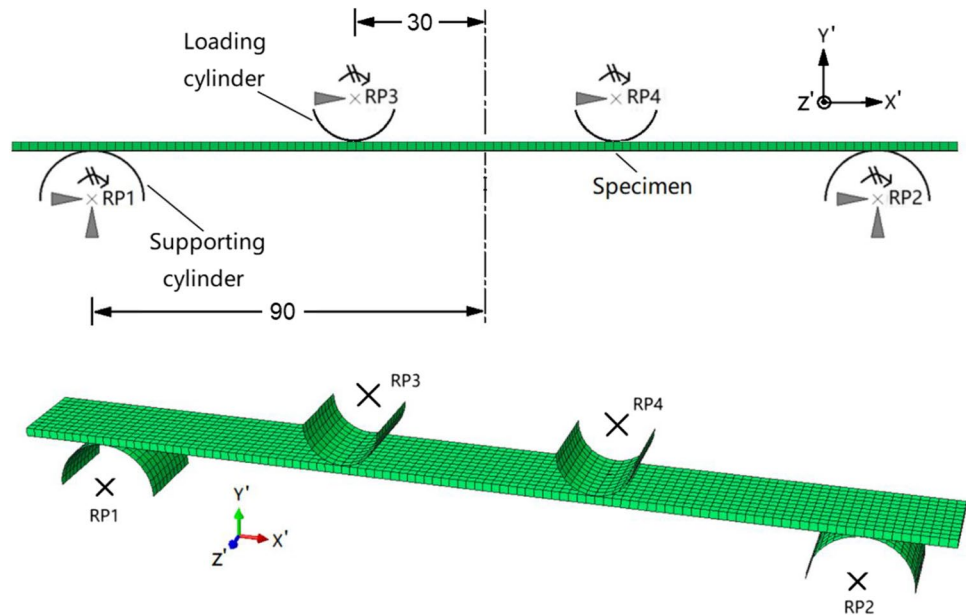
after 4 iterations, the CAFed sheets satisfied the tolerance range of 0.56 mm with shape error of 0.5 mm for 2 mm and 0.38 mm for 4 mm. The adjustment factors were derived with values greater than 1 for both thicknesses, indicating that lower stiffness of the structure was induced for both thicknesses when loading with flexible tool than the proposed uniform stress bending model. With increasing iteration, the adjustment factor increased for both thicknesses, but the increasing rate gradually decreased. This decreasing trend of the rate demonstrated that the factor was converging to an appropriate value to reflect the true relationship between the deflection and the generated moment with the increase of iterations.

In this study, the initial value of adjustment factor was set to 1 to investigate the proposed method. In practical fabrication, the initial value can be set based on FE simulation. As demonstrated in Fig. 13a and b, the FE simulation results are close to the experimental data. Therefore, by combining FE analysis as preliminary estimation, a more proper initial value greater than 1 can be adopted to decrease the required iterations for the target shape and to improve the cost efficiency when deforming with flexible tool.

6 Conclusions

In this study, a closed-form solution for creep age forming springback prediction covering elastic to plastic behaviours of the material has been proposed. Based on the solution, a springback compensation method for CAF fabrication with complex flexible forming tool has been developed. Both the proposed solution and the compensation method have been verified with corresponding CAF tests adopting the latest 3rd generation Al-Li alloy. Major conclusions can be summarised as:

(1) Due to superior strength and creep resistance of the Al-Li alloy, a large loading displacement is required and a high springback percentage has been observed in CAF fabrication of a singly curved sheet with curvature of 1/2000 mm^{-1}. When adopting flexible tool, the loading displacement was 12.9 and 7.4 times larger than the target deflection with springback percentage of 92.9% and 87.4% respectively for the 2 and 4 mm sheets, which noticeably raised the difficulty of springback prediction and compensation.

Table 7 Summary of the four-point bending FE model and boundary conditions

Part	Element type	Element size	Boundary conditions	Surface contact	Friction coefficient
Loading cylinder	Discrete rigid	2×2 mm	All fixed apart from $U_{y'}$	Cylinder-specimen	0.25
Supporting cylinder	Discrete rigid	2×2 mm	All fixed	Cylinder-specimen	0.25
Specimen	S4R	2×2 mm	None	Specimen-cylinder	0.25

(2) A closed-form springback prediction solution is developed by combining the traditional beam theory and Winkler's theory, for CAF covering deformation from elastic to plastic loadings. Furthermore, an efficient springback compensation method for CAF is proposed based on the developed solution method.

(3) Good convergences have been achieved among the results from the developed prediction solution, FE simulation, and experiments for four-point bending CAF tests, conducted in both elastic and plastic loading ranges with different sheet thicknesses. The validity of the proposed closed-form springback prediction solution has been well supported with a maximum error of 0.49 mm compared with the experimental results.

(4) Successful CAF fabrication of target single-curvature sheet using multipoint flexible tool has been achieved by utilising the proposed springback compensation method within four iterations and with acceptable tolerances. An adjustment factor greater than 1 has been obtained for both 2 and 4 mm sheets in CAF with flexible tool, indicating a lower stiffness structure has been induced when loading with flexible tool than the proposed uniform stress bending model.

(5) The applicability of the developed springback prediction solution and the solution-based compensation method in plastic loading, verified through corresponding CAF tests, has extended the application area beyond the traditional beam theory-based prediction and compensation methods to elastic–plastic CAF covering cases of large deflection in plastic range.

Appendix 1

Derivation of Eq. (18)

Based on Eq. (12), r_i and r_o can be expressed as functions of R_{n3}, i.e. $r^* = f_1(R_{n3})$:

$$r^* = \frac{-B' + \sqrt{B'^2 - 4A'C'}}{2A'}, r^* = r_i \ or \ r^* = r_o \tag{26}$$

where A', B', and C' are derived as:

$$\begin{cases} A' = \varepsilon_y \theta_2 \\ B' = \Delta\theta t/2 - R_{n2}\theta_2\varepsilon_y - \theta_2\varepsilon_y t/2 \\ C' = -\Delta\theta R_{n3} t/2 \end{cases} \tag{27}$$

with determined ε_y, θ_2, $\Delta\theta$, t, and R_{n2}.

By substituting Eqs. (13) and (15) into Eq. (17), as the following equation can be obtained:

$$\int_{R_{n2-\frac{t}{2}}}^{R_{n2}+\frac{t}{2}} \sigma \, dr = \int_{r_i}^{r_0} \sigma_e \, dr + \int_{r_i}^{R_{n2}+\frac{t}{2}} \sigma_p \, dr + \int_{r_0}^{R_{n2}+\frac{t}{2}} \sigma_p \, dr = A'' + B'' + C'' = 0 \tag{28}$$

where A'' is derived as:

$$A'' = \int_{r_i}^{r_0} \sigma_e \, dr = \varepsilon_y \left(\frac{t}{2}\right)^{-1} \frac{r^2}{2} \bigg|_{r_i}^{r_0} - \varepsilon_y \left(\frac{t}{2}\right)^{-1} R_{n2} r \bigg|_{r_i}^{r_0}$$
$$+ \ln(r)\left(\triangle\theta \frac{(r - R_{n3})}{\theta_2}\right)\bigg|_{r_i}^{r_0} - \ln(r)\left(\frac{\triangle\theta}{\theta_2}\right)\bigg|_{r_i}^{r_0} \tag{29}$$

By adopting Eq. (15) and applying Taylor expansion, B'' can be derived as:

$$B'' = \int_{r_i}^{R_{n2}-\left(\frac{t}{2}\right)} \sigma_p \, dr = \sigma_y r \bigg|_{r_i}^{R_{n2}-\frac{t}{2}} + h\left(\frac{\triangle\theta}{\theta_2}\right)^n \left(r\bigg|_{r_i}^{R_{n2}-\frac{t}{2}} - nR_{n3}\ln(r)\bigg|_{r_i}^{R_{n2}-\frac{t}{2}} - \frac{n(n-1)R_{n3}^2}{2r}\bigg|_{r_i}^{R_{n2}-\frac{t}{2}} + \frac{n(n-1)(n-2)R_{n3}^3}{12r^2}\bigg|_{r_i}^{R_{n2}-\frac{t}{2}}\right) \tag{30}$$

Similarly, C'' is expressed as:

$$C'' = \int_{r_0}^{R_{n2}+t/2} \sigma_p \, dr = \sigma_y r \bigg|_{r_0}^{R_{n2}+t/2} + h\left(\frac{\Delta\theta}{\theta_2}\right)^n \left(r\bigg|_{r_0}^{R_{n2}+t/2} - n R_{n3}\ln(r)\bigg|_{r_0}^{R_{n2}+\frac{t}{2}} - \frac{n(n-1)R_{n3}^2}{2r}\bigg|_{r_0}^{R_{n2}+\frac{t}{2}} + \frac{n(n-1)(n-2)R_{n3}^3}{12r^2}\bigg|_{r_o}^{R_{n2}+\frac{t}{2}}\right) \tag{31}$$

where h and n are determined material constants; Eq. (17) or (28) can be expressed as a function of R_{n3} as Eq. (18), i.e. $f(R_{n3})= 0$.

However, the derived function cannot be solved analytically to obtain the solution of $\underline{R_{n3}}$. Bisection method is applied as an iterative algorithm tool to approach the value of R_{n3}. The process of utilising bisection method to obtain the value of R_{n3} is manifested in Fig. 14. Considering the possible extent of deflection increase from $a_2 b_2 c_2 d_2$ to $a_3 b_3 c_3 d_3$ in CAF and corresponding potential neutral plane variation range in plastic loading state, in the first iteration, the initial values of $R_{n3a}{}^i$ and $R_{n3b}{}^i$, as the upper and lower limits of R_{n3} for bisection method, are given with values as $R_{n3a}^1 = R_{n2} + t/5$ and $R_{n3b}^1 = R_{n2} - t/5$. Tol_2 is defined as the error tolerance comparing with obtained results of $f(R_{n3})$, which is set to be the value of 5E-4 in this study.

Appendix 2

Adopted constitutive model

The constitutive equations adopted in this study are shown below [34]:

$$\dot{\varepsilon}_c(t_a) = A_3 sinh\big(B_1(\sigma(t_a) - \sigma_{th})(1 - H)^{n_2}\big) \tag{32}$$

$$H = k_1'\big(\overline{\rho} - \overline{\rho}_0\big) + k_2'\overline{r} \tag{33}$$

$$\varepsilon_p' = (\sigma - \sigma_{end})/E' + K\big(\sigma - \sigma_{end}\big)^{n'} \tag{34}$$

$$\dot{\overline{\rho}}_0 = A_1(1 - \overline{\rho}_0)\big|\dot{\varepsilon}_p'\big|^{m_1} - C_p\overline{\rho}_0^{m_2} \tag{35}$$

$$\sigma_{th} = \sigma_{th_0}/(1 + exp\big(n_{1a}\overline{\rho}_0^{m_{1a}} - B\big)) \tag{36}$$

$$\dot{\overline{\rho}} = A_1(1 - \overline{\rho})\big|\dot{\varepsilon}_c\big|^{m_1} - C_p\overline{\rho}^{m_2} \tag{37}$$

$$\dot{\overline{r}} = C_r\big(Q - \overline{r}\big)^{m_3}\big(1 + \gamma_0\overline{\rho}^{m_4}\big) \tag{38}$$

where $\varepsilon_c(t_a)$ and $\sigma(t_a)$ are respectively the creep strain and stress at layer r at creep-ageing time t_a; is the threshold stress; H is a creep variable to reflect the hardening effect induced by evolution of normalised dislocation density $\overline{\rho}$ and normalised precipitate radius $\overline{r}$ during creep-ageing. ε_p' and $\overline{\rho}_0$ are respectively the plastic strain and the normalised dislocation density accumulated in the loading stage. Other symbols used in the equations are material constants. The dot above a symbol indicates time derivative. The initial values and material constants used for the constitutive equations are presented respectively in Appendix Table 5 and Appendix Table 6.

Appendix 3

Four-point bending FE model

As shown in Fig. 15, a three-dimensional ABAQUS FE model was established according to the setup and dimensions in Fig. 7a. The constitutive model was implemented in the simulation through CREEP subroutine. For the loading cylinders, as shown in Fig. 15, freedom for all directions apart from displacement along y' ($U_{y'}$) axis was fixed, allowing the loading cylinders only move parallelly along y' axis. The supporting cylinders were completely fixed in all directions. Surface contacts were set up between the cylinders and specimen which were modelled with penalty tangential behaviour with friction

coefficient of 0.25. The specimen was composed of S4R shell element with mesh size of 2×2 mm and 11 integration points through the thickness direction. The cylinders were composed of discrete rigid elements with size of 2×2 mm. The general information of the model is summarised in Appendix Table 7. During simulation, the specimen was deformed by the loading cylinders with the designed loading displacement (given in Tables 2 and 3) and was kept at the obtained shape for creep-ageing with the required time. The final defection prediction result was obtained after the specimen was fully unloaded with the upward movement of the loading cylinders.

Declarations

Competing interests The authors declare no competing interests.

References

1. Zhan L, Lin J, Dean TA (2011) A review of the development of creep age forming: experimentation, modelling and applications. Int J Mach Tools Manuf 51:1–17
2. Li Y, Shi Z, Lin J, Yang YL, Rong Q, Huang BM et al (2017) A unified constitutive model for asymmetric tension and compression creep-ageing behaviour of naturally aged Al-Cu-Li alloy. Int J Plast 89:130–149
3. Lin J, Ho KC, Dean TA (2006) An integrated process for modelling of precipitation hardening and springback in creep age-forming. Int J Mach Tools Manuf 46:1266–1270
4. Yang Y, Zhan L, Liu C, Wang X, Wang Q, Tang Z et al (2020) Stress-relaxation ageing behavior and microstructural evolution under varying initial stresses in an Al–Cu alloy: Experiments and modeling. Int J Plast 127:102646
5. Lam AC, Shi Z, Lin J, Huang X, Zeng Y, Dean TA (2015) A method for designing lightweight and flexible creep-age forming tools using mechanical splines and sparse controlling points. Int J Adv Manuf Tech 80:361–372

6. Zhang L, Li H, Bian T, Wu C, Gao Y, Lei C (2021) Advances and challenges on springback control for creep age forming of aluminum alloy. Chin J Aeronaut 35:8–34. https://doi.org/10.1016/j.cja.2021.10.019

7. Wagoner H, Lim H, Lee MG (2013) Advanced issues in springback. Int J Plast 45:3–20

8. Chan KC, Wang SH (1999) Theoretical analysis of springback in bending of integrated circuit leadframes. J Mater Process Technol 91:111–115

9. Wenner ML (1983) On work hardening and springback in plane strain draw forming. J Appl Metalwork 2:277–287

10. Ma J, Welo T (2021) Analytical springback assessment in flexible stretch bending of complex shapes. Int J Mach Tools Manuf 160:103653

11. Choi J, Lee J, Bong H, Lee M, Barlat F (2018) Advanced constitutive modeling of advanced high strength steel sheets for springback prediction after double stage U-draw bending. Int J Solids Struct 151:152–164

12. Xue X, Liao J, Vincze G, Gracio J (2015) Modelling of mandrel rotary draw bending for accurate twist springback prediction of an asymmetric thin-walled tube. J Mater Process Technol 216:405–417

13. Gordan J (2021) On pure bending in non-linear elasticity: a circular closed-form 2D solution for semi-linear orthotropic material. Eur J Mech A Solids 90:104289

14. Ma J, Li H, Fu M (2021) Modelling of springback in tube bending: a generalized analytical approach. Int J Mech Sci 204:106516

15. Zhang S, Fu M, Wang Z, Fang D, Lin W, Zhou H (2021) Springback prediction model and its compensation method for the variable curvature metal tube bending forming. Int J Adv Manuf Tech 112:3151–3165

16. Meng Q, Zhao J, Mu Z, Zhai R, Yu G (2022) Springback prediction of multiple reciprocating bending based on different hardening models. J Manuf Process 76:251–263

17. Sallah M, Peddieson J, Foroudastan S (1991) A mathematical model of autoclave age forming. J Mater Process Technol 28:211–219

18. Narimetla SP, Peddieson J, Buchanan GR, Foroudastan S (2000) A simple unified age forming model. Mech Res Commun 27:631–636

19. Jeunechamps P, Ho KC, Lin J, Ponthot J, Dean TA (2006) A closed form technique to predict springback in creep age-forming. Int J Mech Sci 48:621–629

20. Li Y, Rong Q, Shi Z, Sun X, Meng L, Lin J (2019) An accelerated springback compensation method for creep age forming. Int J Adv Manuf Tech 102:121–134

21. Gan W, Wagoner RH, Mao K, Price S, Rasouli F (2004) Practical methods for the design of sheet formed components. J Eng Mater Technol 126:360–367

22. Seo Y, Park J, Song W, Kang B, Kim J (2014) Flexible die design and springback compensation based on modified displacement adjustment method. Adv Mech Eng 6:131253

23. Yang X, Ruan F (2011) A die design method for springback compensation based on displacement adjustment. Int J Mech Sci 53:399–406

24. Lingbeek RA, Gan W, Wagoner RH, Meinders T, Weiher J (2008) Theoretical verification of the displacement adjustment and springforward algorithms for springback compensation. IntJ Mater Form 1:159–168

25. Wang Z, Hu Q, Yan J, Chen J (2017) Springback prediction and compensation for the third generation of UHSS stamping based on a new kinematic hardening model and inertia relief approach. Int J Adv Manuf Tech 90:875–885

26. Cheng H, Cao J, Xia Z (2007) An accelerated springback compensation method. Int J Mech Sci 49:267–279

27. Bodily B, Heinimann M, Bray G, Colvin E et al (2012) Advanced aluminum and aluminum-lithium solutions for derivative and next Generation aerospace structures. SAE Technical Paper 2012-01-1874. https://doi.org/10.4271/2012-01-1874

28. Abd A, Xu Y, Guo X, Zhang S, Ma Y, Chen D (2018) Strengthening mechanisms, deformation behavior, and anisotropic mechanical properties of Al-Li alloys: a review. J Adv Res 10:49–67

29. Wang X, Rong Q, Shi Z, Li Y, Cao J, Chen B et al (2022) Investigation of stress effect on creep, precipitation and dislocation evolution of Al–Li alloy during creep age forming. Mater Sci Eng, A 836:142723

30. Li Y, Shi Z, Rong Q, Zhou W, Lin J (2019) Effect of pin arrangement on formed shape with sparse multi-point flexible tool for creep age forming. Int J Mach Tools Manuf 140:48–61

31. Li Y, Shi Z, Lin J, Yang Y-L, Saillard P, Said R (2018) Effect of machining-induced residual stress on springback of creep age formed AA2050 plates with asymmetric creep-ageing behaviour. Int J Mach Tools Manuf 132:113–122

32. Ye J (2015) Structural and stress analysis: theories, tutorials and examples, 2nd edn. CRC Press. https://doi.org/10.1201/b20513

33. Hwang S, Lee J, Yang Y, Yoo M (2010) Springback adjustment for multi-point forming of thick plates in shipbuilding. Comput Aided Des 42:1001–1012

34. Wang X, Rong Q, Shi Z, Lin J (2022) Improved creep behaviour for a high strength Al-Li alloy in creep age forming: experimental studies and constitutive modelling. Int J Plast 103447